Article

Label-Free Multiplexed Electrical Detection of Cancer Markers on a Microchip Featuring an Integrated Fluidic Diode Nanopore Array

Lian Duan, and Levent Yobas

ACS Nano, **Just Accepted Manuscript** • DOI: 10.1021/acsnano.8b02260 • Publication Date (Web): 19 Jul 2018

Label-Free Multiplexed Electrical Detection of Cancer Markers on a Microchip Featuring an Integrated Fluidic Diode Nanopore Array

*Lian DUAN and Levent YOBAS**

Department of Electronic and Computer Engineering, The Hong Kong University of Science and Technology, Clear Water Bay, Kowloon, Hong Kong SAR, China

*Address correspondence to eelyobas@ust.hk

ABSTRACT

We introduce an integrated array of glass nanopores on a silicon microchip fabricated in a batch process through low-resolution photolithography and standard semiconductor processing tools. By functionalizing each nanopore against a distinct target, we further demonstrate ultrasensitive, label-free, multiplexed electrical detection of cancer-marker proteins in real time through charge-dependent ionic current rectification. As nanofluidic diode biosensors, the nanopores return rapid results with a limit of detection reaching concentrations as low as attomolars in assay buffer and femtomolars in undiluted untreated human serum, a rare achievement for this class of nanosensors. Multiplexed detection capability has been demonstrated on proteins carcinoembryonic antigen, alpha-fetoprotein antigen, and human epidermal growth factor receptor-2 with the assay further scalable to a size that is limited by the readout electronics. The nanopores are also found with a considerably advanced detection limit as well as dynamic range in relation to the nanoslit counterparts, validated by the measurements on cardiac protein troponin T. This highly robust assay platform draws from rich nanopore physics and could provide further enhanced detection through concentration polarization, subsequent target enrichment and serum desalting, all potentially induced by the nanopores presently redundant in the array. This integration would be crucial for removing major obstacles to the practical use of the nanopore-based assays.

Keywords

nanofluidic diode, biosensor, ionic current rectification, multiplexing, biomarker, nanopore

Cancer continues to be a leading cause of death worldwide despite the recent advances in the field of proteomics and genomics,[1,2] partly due to the lack of technologies to bring those advances to the clinics and bedside for early diagnosis and prognosis of the disease. Robust technologies are also required in precision or personalized medicine to deal with the complexity of the disease among populations through rapid and multiplexed detection of many biomarkers with high selectivity and sensitivity. The disease heterogeneity renders single-biomarker tests inadequate for accurate assessment, and thus assaying a panel of biomarkers is of utmost value.[3] Enzyme-linked immunosorbent assay (ELISA), the method of choice in clinical settings for detecting biomarkers, rather falls short of meeting these new demands.[4]

Miniaturization under the umbrella of nanotechnology has shown great potential with revolutionary biosensors based on plasmonic nanoparticles,[5] nanocantilevers,[6] carbon nanotubes,[7] semiconductor nanowires[8-10] and nanobelts,[11] and nanofluidics.[12] Of those, label-free field-effect biosensors have particularly received much attention for merits like rapid response, ultralow detection limit, scalability and portability, and high-volume manufacturability. For instance, nanowire field-effect transistors are known to exhibit ultrasensitivity for detecting low-abundance biomarkers such as nucleic acids,[13] proteins,[8] and single virus complexes[10] in buffer or serum by a simple electrical readout. These sensors can also be configured into clusters for multiplexed detection of a panel of biomarkers.[9]

A recent addition to the family of field-effect biosensors exploits physics around the electrical double layer (EDL) that is often influential within highly confined spaces like the nanopores (nanochannels). Permselectivity, the preferential permeation of ions,

encountered within the nanopores gives rise to the ion concentration polarization and space charge formation in aqueous buffer under an externally applied bias.[14-16] Depending on the bias polarity, ions get accumulated or depleted inside the nanopores when an asymmetry is introduced either in the structural profile,[17] or the surface charge,[18] or in the form of a lopsided buffer ionic strength.[19] All these factors contribute to nonlinear current-voltage ($I-V$) characteristics reminiscent of those encountered in semiconductor physics, and hence the terms nanofluidic diodes or transistors associated with the nanopores and nanoslits. Nanofluidic diode characteristics, *i.e.,* suppressed ionic current under the reversed bias polarity (rectified $I-V$ curves) have been extensively studied using membrane pores ion-track etched,[20] or lithographically etched,[21] as well as glass nanopipette tips (pulled capillaries).[22] These $I-V$ characteristics, especially the degree of rectification, are shown extremely sensitive to the nanopore EDL and thereby greatly influenced by the electric charge of nearby species.[15,23] The membrane pores and the nanopipette tips being functionalized with surface receptors have been studied for biosensor characteristics against various targets such as DNA oligomers,[24] cancer-marker proteins,[22] amino acids,[25] metal ions and metal ion-molecular complexes,[26] as well as small molecules as in aptamer-based cocaine sensing.[27] In those studies, however, the limit of detection is found barely reaching below picomolar levels.

We previously reported a nanofluidic diode biosensor integrated on a microchip with microfluidics and demonstrated selective and rapid detection of cardiac protein marker troponin in buffer and serum at femtomolar concentrations.[28] Unlike discrete counterparts (*e.g.*, nanopipette tips, track-etched membrane pores), this integrated unit is highly robust and offers well-defined functional sites. However, the achieved limit of detection, albeit

considerably improved, does not reflect the true capacity of this transduction mechanism, which is due to the usage of multiple nanoslits instead of a single isolated nanopore. Here, we further refine our integration approach and demonstrate a single-nanopore biosensor with substantially advanced performance metrics in relation to the nanoslit counterpart; the limit of detection and dynamic range are improved at least by an order of magnitude. More importantly, rendering such nanopores addressable on a microchip, we further demonstrate a label-free multiplexed electrical detection of three cancer markers rapidly in the assay buffer as well as in undiluted untreated human serum. Ultrasensitivity and high selectivity achieved in this study are comparable or better than those reported for the field-effect nanosensors (*e.g.*, nanowires). Notably, the nanopore integration is independent of advanced patterning techniques and relies solely on low-resolution photolithography and standard semiconductor processes, a key aspect for a smooth transition of this technology to the bedside and clinical tests.

RESULTS AND DISCUSSION

Concept. Figure 1a describes multiplexed detection of biomarkers using nanopores as nanofluidic diodes where each is functionalized against a specific cancer protein marker with corresponding monoclonal antibodies (mAbs) immobilized on the nanopore and surroundings (active site). As described in Figure 1b, the $I-V$ curves of the nanopores are modulated by the electric charge of the target proteins being captured by mAbs. A patterned passivation layer (silicon nitride) placed outside the active sites prevents potential loss of low-abundance markers through nonspecific surface adsorptions. The nanopores are defined by a doped glass film featuring a nonconformal step coverage

profile over a structured silicon substrate and thereby contributing to the asymmetric (conical) pore profile that is essential for a rectified $I - V$ characteristic. Figure 1c briefly explains the construction of the nanopores, which is further detailed in Methods as well as in Supporting Information (Figure S-1).

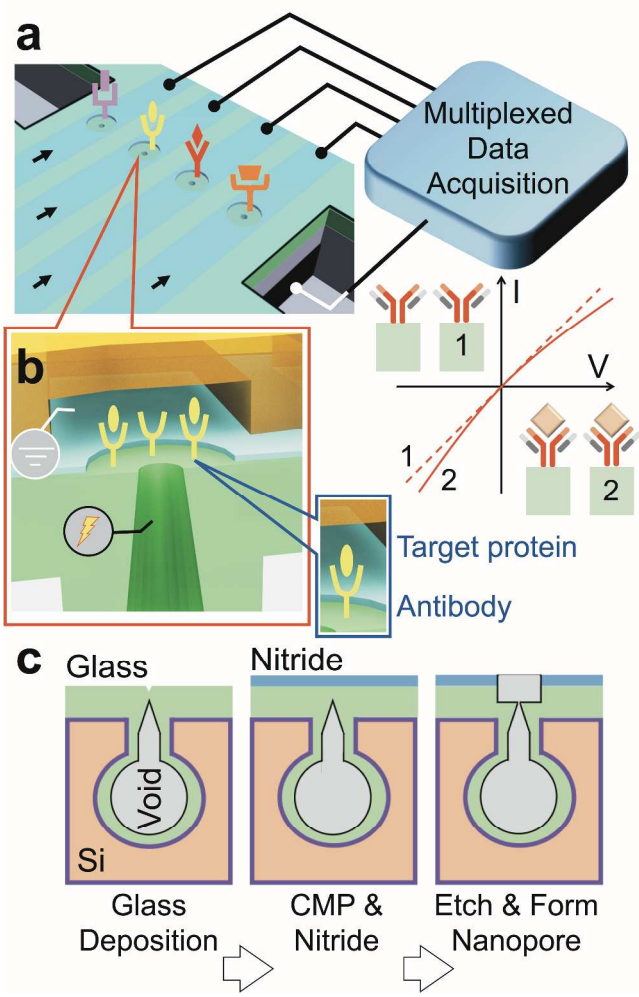

Figure 1. Illustrations. (a) Multiplexed detection of target protein markers using a row of nanopores integrated on a microchip as nanofluidic diode biosensors. The nanopores receive the sample through dedicated fluidic channels (arrows) for independent referencing and readout while being driven by the voltage bias through a common channel underneath. Each nanopore is selective to a specific target protein owing to

capture mAbs immobilized on the surface. (b) The nanopore biosensing concept based on the rectified $I - V$ curve with the degree of rectification modulated by the presence of the captured charged proteins. (c) Fabrication process briefly described on a nanopore cross-section view illustrated after key steps.

Structure. The overall device configuration is schematically described in Figure 2a. The device inherits the multi-layer crossed-channel architecture from the previous nanoslit array diode.[28] In this architecture, a row of nanoslits/nanopores is situated on a silicon bridge, which is monolithically integrated over a fluidic "recording" channel, and the nanopores directly open up to fluidic "sample" channels moulded in an elastomer cover (polydimethylsiloxane, PDMS). Each sample channel is coupled to the recording channel through the respective nanopore exclusively, and features a channel width of 8 μm, which is comparable to the nanopore pitch to facilitate the inclusion of a single nanopore during device assembly (Figure 2b). Although many of the nanopores become inaccessible after the assembly, such redundancy is adopted for the ease of manual alignment. The nanopores are interconnected to the channel underneath, through buried cavities depicted in a cross-sectional profile in Figure 2c. The cavities are conveniently formed in silicon by tailoring the etch profile in a single photomasking process (Supporting Information, Figure S-1). The nanopores are self-formed structures and exhibit a conical profile at a tapering angle of ~18° (Figure 2d). The structures arise from partial removal of a doped glass film (phosphosilicate glass, PSG) deposited with a non-conformal thickness profile that is thick enough to pinch off 3-μm-wide silicon well openings. Despite the use of low-resolution photolithography, this approach yields nanopores with a nominal diameter of

50 nm (Figure 2d, inset) and a size distribution of 51.3 ± 5.5 nm, (n~100, Figure 2e). Such size variation, albeit of a concern, is rather small in consideration of the dimensional uncertainties inherent within the process. In particular, the deposition and partial removal of the PSG layer are the key contributors to the resulting size distribution. Though further process optimization is in order, the nanopores considered here fall in the close vicinity of the nominal value. The size variation can be further addressed by further scaling down the silicon wells without resorting to low-throughput patterning techniques. This would lead to a drastic reduction in the thickness requirement of PSG that needs to be deposited as well as partially removed, thereby leading to a reduced size variation.

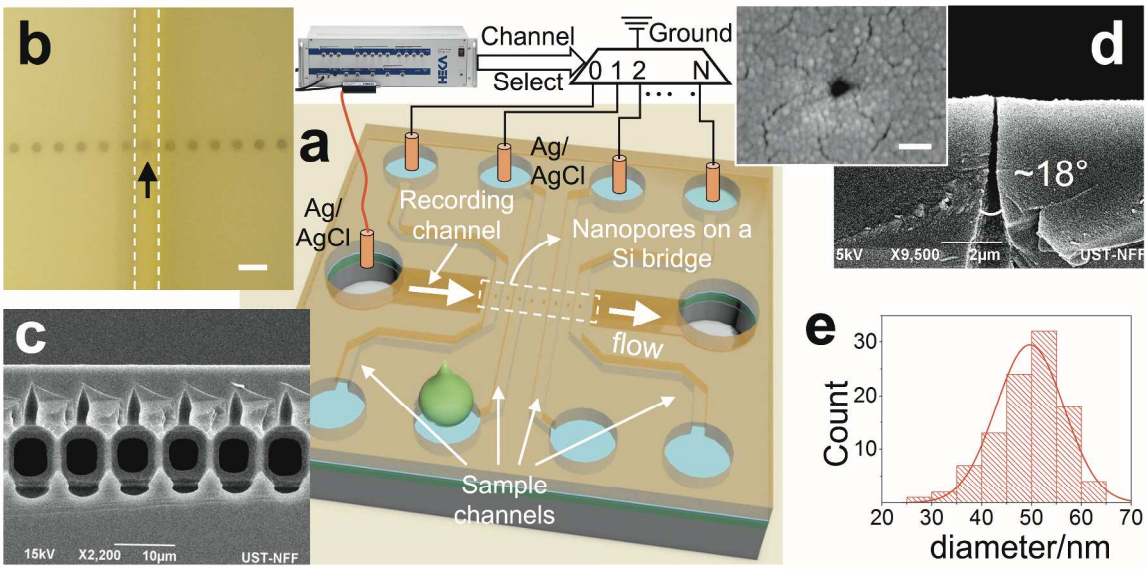

Figure 2. (a) Illustration of the integrated nanopore biosensor and measurement setup. (b) Photomicrograph showing a section of the nanopores with a single nanopore (arrow) captured inside a sample channel (dashed lines). (c,d) Scanning electron micrographs of (c) the nanopores and (d) a single nanopore tip end both shown in sectioned views (inset: a single nanopore shown in a plane view). (e) The size distribution of the nanopores.

Scale: (b) 5 μm; (c) 10 μm; (d) 2 and 1 μm (inset). Dark regions in (c) signify the buried cavities interconnecting the nanopore row to the recording fluidic channel.

Diode Characteristics. Figure 3 presents the nanopore rectification characteristics ($I-V$ curves) acquired for distinct ionic strengths and pH levels of the electrolyte (KCl or PBS) placed in both the sample as well as the recording channels. The insets show the degree of rectification, R, based on the definition $R = log_2(I_{+1V}/I_{-1V})$, with I_{+1V} and I_{-1V} being the positive and negative current intensities at fixed bias voltage levels of ±1 V.[29] Here, the voltage bias (anode or cathode) refers to the Ag/AgCl wire electrode facing the nanopore base whereas the reference (ground) to a second Ag/AgCl facing the nanopore tip. The rectification is relatively weak in an acidic pH, 2, ($R\sim -0.2$) due to the nanopore surface charge being quenched and yet it becomes noticeable in neutral and an alkaline pH, 11, ($R\sim -0.6$, and $R\sim -0.8$, respectively) because the surface acquires excess negative charge (Figure 3a). Likewise, the rectification depends on the solution ionic strength (Figure 3b); it is more pronounced at low ionic strengths (0.01× PBS, $R\sim -1.6$), than at high ionic strengths (1× and 0.1× PBS, $R\sim -0.65$, and $R\sim -0.84$, respectively). This is because the nanopore surface charge is screened by a thin EDL ($\lesssim$ 1 nm) in the former as opposed to a thick EDL influential across the nanopore tip end in the latter.

The effect of the solution ionic strength on the nanopore rectification can be further seen in a conductance plot derived from the respective $I-V$ curve (Figure 3c). The nanopore conductance shows only a slight increase with the increased bias strength under the positive bias polarity but a drastic rise occurs under the reversed-polarity bias. The

favored polarity is in line with the excess negative surface charge of the nanopore at pH, 7.4, and corroborates previous studies.[30] Numerical studies have revealed that the rectification arises from a broken symmetry (*e.g.*, conical profile) and the permselectivity of the nanopore, which collectively introduce asymmetric ionic fluxes and thus bring enrichment or depletion of ions inside the nanopore tip region (diagrams, Figure 3c). Because the externally introduced electric field (set by the applied bias) interacts more strongly with a thicker EDL around the nanopore tip end, the asymmetry is pronounced at low ionic strengths (comparison of 0.01× PBS *vs.* 1× PBS in Figure S-2).

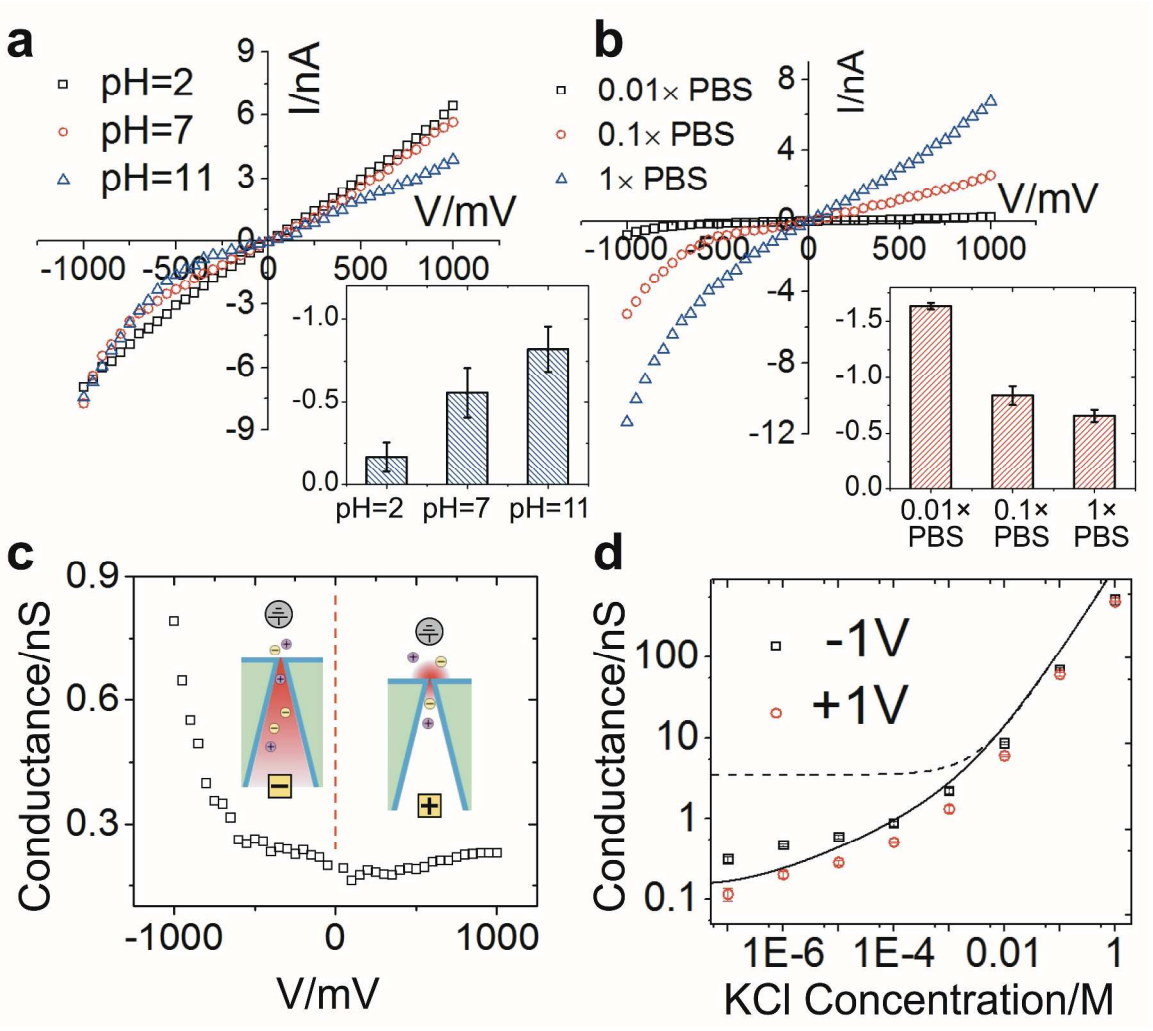

Figure 3. (a,b) Rectification characteristics ($I - V$ plots) of single nanopores at specific (a) pH values (background electrolyte 10 mM KCl) and (b) ionic strengths (PBS, pH 7.4). The charts (insets) present the rectification ratios R from comparable nanopores. Error bars: ±1 s.d. ($n = 5$). (c,d) Nanopore conductance plots as a function of (c) the applied bias (0.01× PBS) and (d) the ionic strength of the background electrolyte (KCl). Line fittings are the values estimated on the basis of a surface charge density either a constant at 60 mC/m^2 (dashed line) or varying in 1 − 60 mC/m^2 based on the aqueous pH and ionic strength (solid line).

At low ionic strengths, the nanopore conductance (under either bias polarity) strongly deviates from those predicted based on the bulk conductivity of the background electrolyte (Figure 3d). This is mainly due to the non-negligible contribution of counterions (EDL) to the overall ionic current. Evaluating this contribution based on a constant surface charge density in the nanopore (dashed line), however, overestimates the nanopore conductance.[31] Instead, a surface-reactivity model, which uses a pH- and salt-dependent surface charge density in consideration of the ions dissociated from the background electrolyte as well as the nanopore surface reasonably describes the nanopore conductance (solid line).[31-33] This model is well described in previous studies where it has been successfully applied to the conductance profile of the nanoslits,[34] silica nanopore,[31] and submicrometer glass capillary array.[35]

Nanopore Biosensors. The nanopores were transformed into biosensors for detecting specific cancer markers by immobilizing respective monoclonal antibodies (mAbs) on the

surface through silane chemistry (Figure 4a). This surface immobilization is exclusive to the nanopores and surroundings (active sites) owing to a patterned passivation layer. Figure 4a also presents a visual confirmation of the immobilization *via* FITC-labeled mAbs. Figure 4b shows representative $I-V$ curves after each functionalization step (0.01× PBS, pH, 7.4) with the direction of rectification paralleling the charge polarities of the respective molecules being immobilized. For instance, the positively charged amine groups of (3-aminopropyl) triethoxysilane (APTES) reverse the rectification polarity after binding to the negatively charged silanol groups of bare nanopore surface (from $R\sim-1.6$ to ~ 0.19). Nearly neutral aldehyde terminals of the linker molecules glutaraldehyde practically negate the rectification brought by the amine groups. The rectification recurs, however, with the subsequent binding of mAbs, in accordance with the net charge of these molecules at the stated pH.

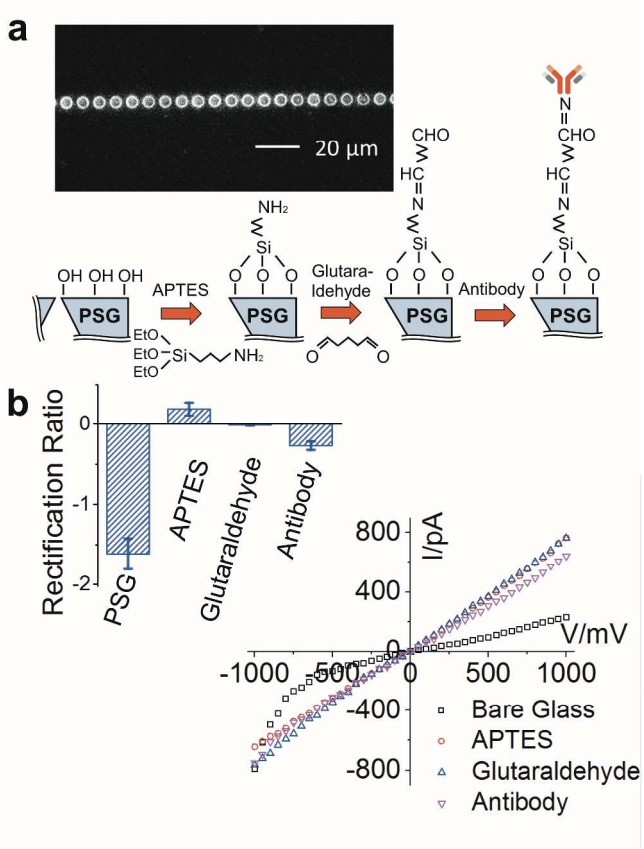

Figure 4. (a) Functionalization procedure for immobilizing mAbs on the nanopores and surroundings (active sites). Fluorescence micrograph shows the active sites immobilized with the FITC-labeled mAbs. (b) $I-V$ curves from a representative nanopore measured after each functionalization step (legend) using 0.01× PBS (pH, 7.4) and the corresponding rectification ratios obtained from comparable nanopores. Error bars: ±1 s.d. ($n = 5$).

Detection in Buffer. The nanopores and the nanoslits share process steps and structural materials, yet mainly differ in geometry. To better understand the role of the geometry in the detection characteristics, the nanopores were first evaluated against the target troponin T (cTnT), a well-known cardiac protein marker also tested on the nanoslit

biosensors previously.[28] For comparison, the measurements were conducted using the same background electrolyte (0.01× PBS) on the nanopores functionalized accordingly.

Figure 5a shows the rectification ratios from four independent nanopores obtained over time during a sequential application of two rounds of cTnT/wash cycles. Representative $I-V$ curves corresponding to cTnT cycles are also shown. While the rectification ratios follow comparable baselines established through the buffer solution lacking the target, the curves shift to distinct plateau levels with the application of cTnT depending on the applied concentration. In the first round, the shift is either negligible or weak for 0.1 and 1 fg/mL (NP1 and NP2) but becomes proportionally noticeable for 10 and 100 fg/mL (NP3 and NP4). In the second round, further shift occurs with the application of a concentration that is four orders of magnitude greater than the previous one. Between the two rounds, the rectification levels endure wash cycles, signifying that each response mainly arises from high-affinity bindings between proteins and mAbs as opposed to non-specific interactions.

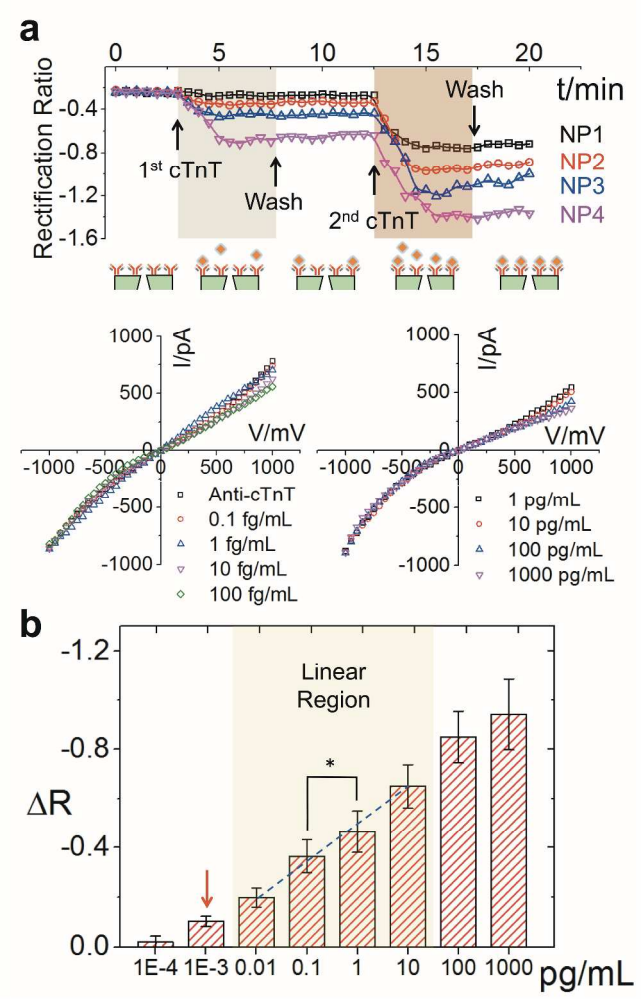

Figure 5. Detection of cardiac marker cTnT in 0.01× PBS (pH, 7.4). (a) Rectification ratio *versus* time data from four nanopores modified with mAbs for cTnT obtained during a sequence of sample and wash cycles. The shaded intervals highlight the sample cycles with the darker interval referring to an elevated target concentration. Nanopore response (NP1, NP2, NP3 and NP4) to a cTnT concentration of 0.1, 1, 10, and 100 fg/mL in the first round and to a concentration of 1, 10, 100, and 1000 pg/mL in the second, respectively. Representative $I-V$ curves associated with the stated concentration levels (legend). (b) Calibration curve of the nanopores for the detection of cTnT in 0.01× PBS (pH, 7.4). The shaded region highlights the dynamic range and the arrow marks the limit

of detection. Error bars: ±1 s.d. ($n = 5$). The * indicates a p-value of <0.05 according to the student's t-test.

Figure 5b shows the calibration plot from cTnT measurements revealing the limit of detection and the dynamic range. ΔR represents the change in the rectification ratio with respect to the baseline, *i.e.*, $\Delta R = R_D - R_0$ where R_D is the rectification ratio obtained for a specific target concentration and R_0 is the baseline prior to the target. The detection limit is noted as 1 fg/mL (~30 aM) based on the respective ΔR value showing a distinct rise over that of 0.1 fg/mL. This value is comparable to the reported detection limit for silicon nanowire field-effect transistors,[36] and an order of magnitude lower than those achieved with the nanoslits.[17] Likewise, the dynamic range spans over three orders of magnitude, ranging from 10 fg/mL to 10 pg/mL, and exceeds the dynamic range of the nanoslits by an order of magnitude. Beyond this range, the concentrations cannot be accurately resolved due to the response saturation. Ultralow detection limits and broad dynamic ranges were similarly observed here for detecting cancer protein markers CEA (1 fg/mL; ~6 aM), AFP (10 fg/mL; ~150 aM), and HER2 (0.1 fg/mL; ~1.5 aM), with each being independently measured at a high purity in 0.01× PBS. (Figure S-3). Although the detection limit here is in the low attomolar range for the specified conditions, this concentration range still corresponds to million(s) of protein copies, which is beyond the realm of detecting few molecules.

For multiplexed detection, equimolar mixtures of the three cancer marker proteins in 0.01× PBS (pH, 7.4) were applied to the nanopores treated with mAbs for CEA (NP1), AFP (NP2) and HER2 (NP3). Figure 6a shows the rectification ratios recorded during sample/wash cycles with each marker applied at a concentration of 100 fg/mL in the first

round and of 100 pg/mL in the second. Initially, the nanopores for CEA (NP1) and AFP (NP2) are shown weakly rectifying as opposed to the nanopore for HER 2 (NP3), which gives a strong positive rectification. All these corroborate the molecular charge of the corresponding mAbs at the stated pH; pI values for anti-CEA,[37] anti-AFP,[38] and anti-HER2 mAbs,[39] are around 6.8, 6.5, and 9, respectively. The injection of the first mixture results in a drastic shift in the rectification of NP3, reversing the polarity, while inducing relatively weak but noticeable shifts in the rectification of NP1 and NP2. Although CEA,[40] and AFP,[41] both having pI, ~4.5, carry more negative charge than HER2 (pI, ~5.6),[39] the drastic response of NP3 might be attributed to rather strong electrostatic interactions between HER2 and the oppositely-charged respective mAbs. All the three nanopores respond comparably to the application of the second mixture. Each response is highly specific; the rectification level endures the subsequent wash cycle, thus ruling out the contributions of the non-specific molecular interactions.

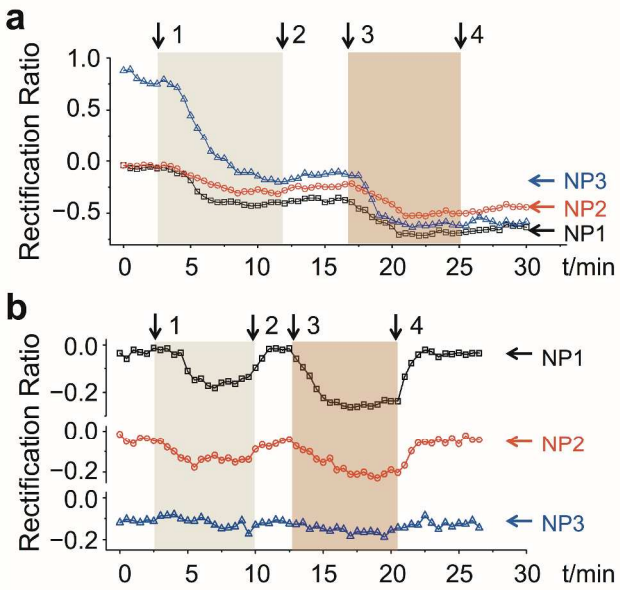

Figure 6. (a) Multiplexed detection of the cancer markers in 0.01× PBS (pH, 7.4) through a nanopore array and (b) the controls revealing negligible mAbs cross reactivity.

Rectification ratio *versus* time data from an array of three nanopores obtained during a sequence of sample (arrows 1 and 3) and wash cycles (arrows 2 and 4). (a) Nanopores (NP1, NP2, and NP3 functionalized with mAbs for CEA, AFP, and HER2, respectively) reacting to an equimolar mixture of the three markers, each at a concentration of 100 fg/mL in the first round and of 100 pg/mL in the second. (b) Nanopores (NP1 and NP2 both functionalized with mAbs for CEA while NP3 passivated with ethanolamine) reacting to AFP (NP1), HER2 (NP2) and CEA (NP3), each independently introduced at a concentration of 100 fg/mL in the first round and of 100 pg/mL in the second. The shaded intervals highlight the sample cycles with the darker interval referring to an elevated target concentration.

Subsequent experiments were performed to evaluate the cross-reactivity of mAbs. Figure 6b shows the rectification ratios obtained from two nanopores (NP1 and NP2) treated with anti-CEA mAbs and a third nanopore (NP3) passivated by reacting surface aldehyde groups with ethanolamine. NP1, NP2, and NP3 were respectively subjected to AFP, HER2, and CEA in 0.01× PBS (pH, 7.4) at a concentration of first 100 fg/mL and then 100 pg/mL after wash. For either concentration, the rectification values of NP1 and NP2 although being shifted with the sample injection, recovers with the subsequent wash, suggesting that the shifts are mainly due to non-specific interactions rather than potential cross-reactivity of mAbs (anti-CEA) for AFP and HER2. No detectable change occurs in the rectification of NP3 with the sample injection, indicating that ethanolamine-blocked surface does not seriously interact with CEA proteins. Similar experiments also revealed no detectable cross-reactivity of anti-AFP and anti-HER2 mAbs for the antigens targeted

(Figure S-4). These controls further support the view that the signals obtained for the targets in the introduced samples are genuine and rather reflect high-affinity bindings than non-specific interactions.

Detection in Serum. Control experiments indicate minor cross-reactivity of mAbs for the target antigens and further suggest that the rectification behavior is specific and being modulated by the target antigens in the test mixtures. These test mixtures, however, are far from being representative of complex clinical samples such as blood serum, which typically presents thousands of distinct proteins with concentrations varying over many orders of magnitude.

Multiplexed experiments were thus subsequently performed using undiluted and untreated human serum. Serum samples were spiked with equimolar mixtures of target markers at various concentrations. High ionic strength of serum samples (~160 mM) and the associated thin EDL hinders the detection, a fundamental issue that incapacitates field-effect biosensors (*e.g.*, nanowires) and is typically addressed by desalting serum.[9] To avoid introducing any sample pretreatment step, the issue was resolved here by displacing the samples with 0.01× PBS subsequent to an incubation period (~20 min) before the measurements. Figure 7 shows the corresponding calibration plots obtained for each cancer marker (the corresponding data set and representative $I - V$ curves for each target concentration are shown in Figure S-5). For serum samples, the limit of detection appears to be on average 1 pg/mL for HER2 (~7.3 fM) and 10 pg/mL for both CEA (~56 fM) and AFP (~150 fM), when gauged against the response levels to the serum samples that were not spiked. The dynamic range in each calibration plot extends over about 3

orders of magnitude. These results set a record for the nanofluidic diode biosensors and put them on par with other ultrasensitive field-effect nanosensors.

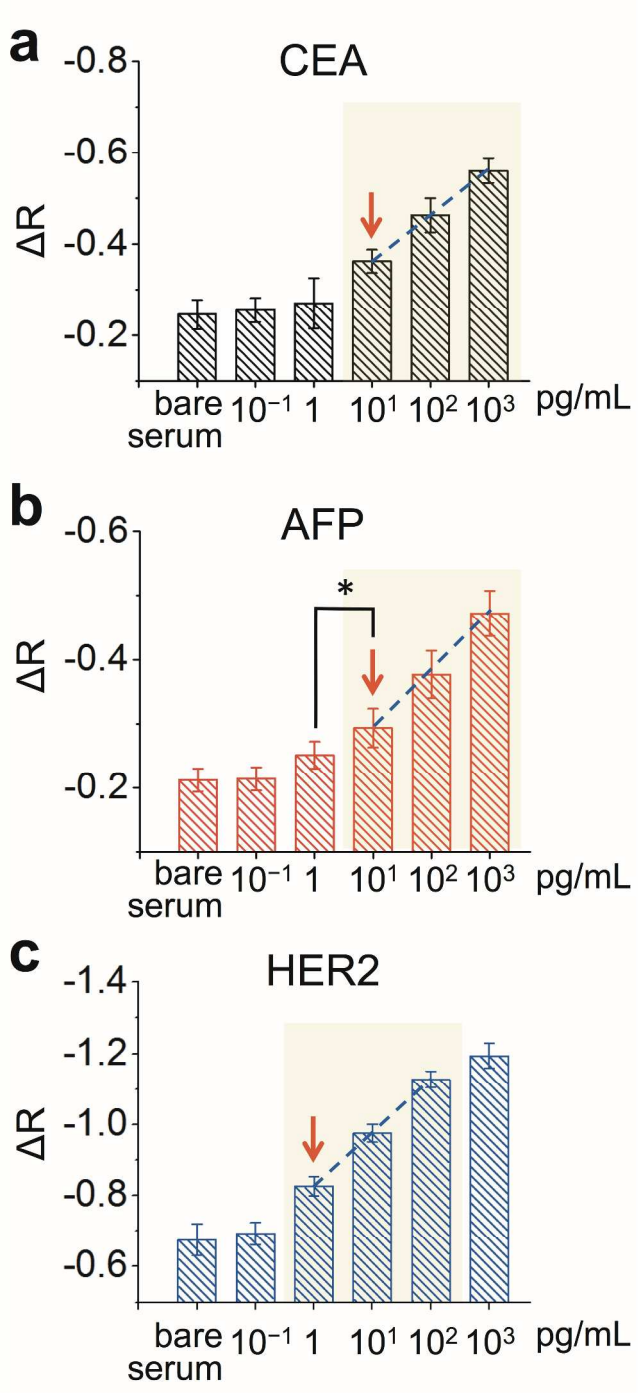

Figure 7. Multiplexed detection of cancer markers in serum using a nanopore array. The calibration curves of the nanopores modified with mAbs for the detection of (a) CEA, (b)

AFP and (c) HER2, in an undiluted and untreated human serum samples. Serum samples were all spiked with an equimolar mixture of CEA, AFP, and HER2 at a concentration of 0.1, 1, 10, 100, and 1000 pg/mL. For each curve, the shaded region highlights the dynamic range and the arrow points at the limit of detection. Error bars: ±1 s.d. ($n = 6$). The * indicates a p-value of <0.05 according to the student's t-test.

The limit of detection values for serum samples in the low femtomolar range exceed those obtained for pure protein samples by orders of magnitude despite the fact that all the measurements were taken using identical buffers (0.01× PBS). The reason for such a large discrepancy, albeit not entirely known, is likely to arise from partial surface recovery of the nanopores after serum exposure. Incomplete removal of adsorbed salt and non-target proteins during wash steps is believed to have altered the surface potential. Further rise in the detection limits are expected as the measurements from multiple nanopores are to be combined to determine target concentration with a precision; this is required due to rather large error bars despite statistical significance ($p < 0.05$). Scaling of the nanopore size and size variation could help enhance the sensor precision.

Figure 8 presents controls for the serum experiments. The rectification ratio time-series plots obtained from the nanopores passivated with ethanolamine (NP1) are shown along with those from the nanopores functionalized with mAbs for any of the three markers (NP2). Both groups exhibit no significant response to human serum samples, in which the targets are present but pre-blocked with an excess of respective mAbs. Contrary, notable shifts occur in the latter plots (NP2) for human serum samples applied without the blocking antibodies. The obtained shifts are possibly due to the presence of the trace

levels of the tumor markers in a healthy human serum. These controls suggest that the nanopores are able to demonstrate high selectivity for the targets in a complex yet clinically relevant sample such as human serum.

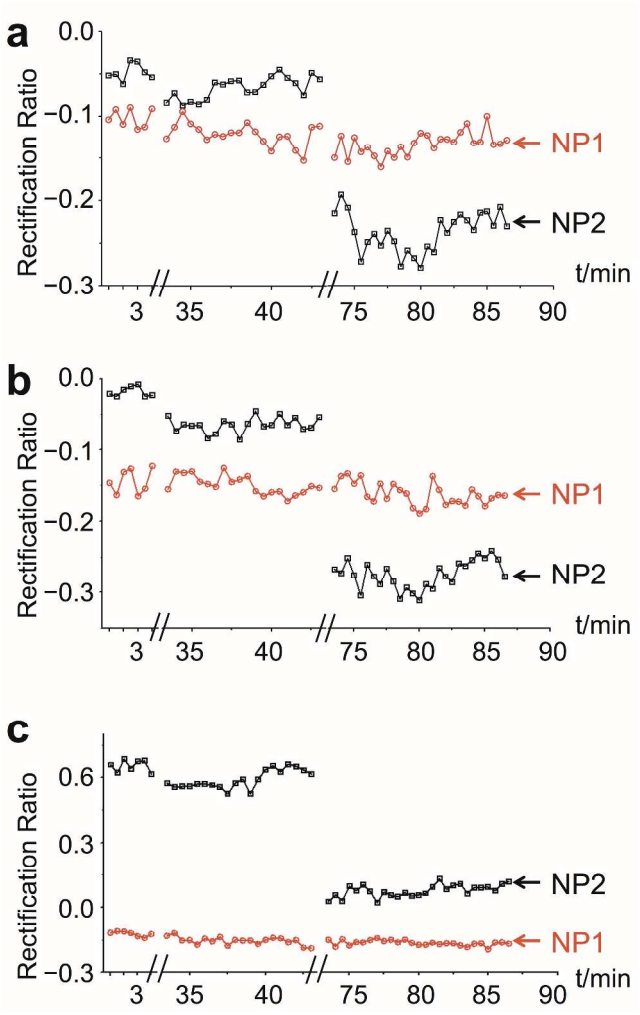

Figure 8. Control experiments using human serum samples on the nanopores passivated with ethanolamine (NP1) and the nanopores functionalized with mAbs (NP2) for (a) CEA, (b) AFP, and (c) HER2. Rectification ratio *versus* time data during a sequence of sample incubation (the discontinuities) and wash cycles (following the discontinuities). Human serum samples were applied in the first cycle with an excess of corresponding

mAbs (10 μg/mL) to block target proteins and then in the second cycle without blocking mAbs. Each sample incubation period lasted about 20 min.

CONCLUSION

We have demonstrated an integrated nanopore biosensor array on a microchip for label-free and multiplexed detection of cancer-marker proteins based on charge-modulated ionic current rectification. Real-time electrical measurements show a highly selective and an ultra-sensitive detection of targets in the assay buffer as well as in undiluted and untreated human serum. Although the multiplexing capability shown here is limited to an array of three nanopores, the assay can be scaled up to accommodate hundreds of nanopores with each featuring surface capture probes for a distinct target protein. The size would be eventually limited by the multiplexing electronics capacity. With the monolithic integration realized here through low-resolution optical lithography and standard semiconductor processes, the presented nanopore biosensors offer an ultra-low detection limit and a dynamic range on par with known nanosensors such as the field-effect nanowire transistors and nanocantilevers.[6,9] An added advantage of using the nanopores for bimolecular detection is that rich nanopore physics (*e.g.*, ion concentration polarization) can be further tapped on to preconcentrate proteins during the incubation, and deplete ions (reduce the ionic strength of serum) during the subsequent signal readout, all controlled electrically.[42] These added functionalities could be realized by dedicated nanoslits/nanopores placed within the array, and could lead to a simplified assay protocol and enhanced robustness, both important aspects for the clinical applications.

MATERIALS AND METHODS

Fabrication. Nanopores and fluidic microchannels were integrated on silicon in a batch process utilizing low-resolution photolithography and standard semiconductor processing tools. The process is briefly described here with key steps as illustrated in Figure S-1. The process was initiated with thermal oxidation of p-type <100> oriented silicon wafers for a 1.5-μm-thick SiO_2 (Step 1). This was followed by photolithography, advanced oxide etch (AOE), and deep reactive ion etch (DRIE) to structure 6-μm-deep wells into silicon at a diameter of 3 μm (Step 2). Further thermal oxidation was performed to insulate the entire structure with a 400-nm-thick SiO_2 layer (Step 3) followed by AOE to expose silicon at the bottom of the wells (Step 4). The removal of silicon from the wells by DRIE first and then by SF_6 plasma etch led to fused buried cavities to interconnect nanopores (Step 5). Buffered oxide etch (BOE) was applied to strip off SiO_2 layer (Step 6) before a further thermal oxidation for a 200-nm-thick SiO_2 insulating layer (Step 7). Low-pressure CVD (LPCVD, 180 mTorr, 420 °C) was carried out for a 5.5-μm-thick layer of phosphosilicate glass (PSG) at a non-conformal step coverage profile to seal off each well while leaving a conical void beneath the surface (Step 8). Chemical mechanical polishing (CMP) was applied to flatten the PSG surface (Step 9) followed by plasma-enhanced CVD (PECVD) for a 300-nm-thick Si_3N_4 layer as chemical surface passivation and then photolithography using the first mask to pattern the passivation layer to open up the active sites (Step 10). Photolithography with a second mask and subsequent AOE and DRIE were performed to create a 30-μm-deep (recording) channel along with the reservoirs (Step 11). Further AOE was applied to remove PSG and open up the nanopores (Step 12). Subsequently, low-temperature thermal oxidation (900 °C, 40 min) was

performed for a 100-nm-thick SiO_2 electrical insulation layer (Step 13). After the functionalization of the nanopores, a PDMS slab featuring (sample) channels along with fluidic ports was aligned and secured in place by clamping (Step 14).

Reagents. The following reagents were procured and used: potassium chloride (KCl), sodium phosphate dibasic (Na_2HPO_4), glutaraldehyde solution, ethanolamine, 3-aminopropyltriethoxysilane (APTES), and human serum (prepared from platelet-poor human plasma) all from Sigma-Aldrich (St. Louis, MO); sodium chloride (NaCl) and bovine serum albumin (BSA) from Sigma Chemicals Co. (St. Louis, MO); potassium dihydrogen phosphate (KH_2PO_4) and potassium hydroxide (KOH) from VWR (Radnor, PA); ethanol absolute from Merck (Kenilworth, NJ); human cardiac troponin T antigens (cTnT) and mAb receptors (anti-FITC labeled) from HyTest (Turku, Finland); and human carcinoembryonic antigen (CEA), alpha-fetoprotein antigen (AFP), and epidermal growth factor receptor-2 (HER2) antigens and mAb receptors (anti-CEA, anti-AFP and anti-HER2) from Shanghai Linc-Bio Science Co., Ltd. (Shanghai, China). 1× PBS solution was prepared according to a standard recipe with the chemicals dissolved in DI wafer and then adjusted to pH ~ 7.4 (composition: 137 NaCl, 2.7 KCl, 10 Na_2HPO_4, and 1.8 KH_2PO_4 all in mM).

Functionalization. Silane chemistry was applied to immobilize mAbs on the glass (PSG) surface within the active sites around the nanopores. A hydroxyl-terminated surface was obtained through oxygen plasma activation after a cleaning step (with a mixture of H_2O_2 and H_2SO_4 1:3 v/v at 120 °C for 20 min, then a copious wash, and a nitrogen blow dry). Subsequent steps were conducted with chemical solutions delivered through fluidic channels moulded in a reversibly attached PDMS slab, except during wash/bake steps. A

solution of ethanol/DI water (95%/5%, v/v) with 2% 3-aminopropyltriethoxysilane (APTES) was delivered for 3 h followed by a copious wash (ethanol/DI water) and bake (120 °C for 1 h), resulting in an amine-terminated surface with APTES covalently linked to the hydroxyl groups. Then, a solution of 2.5% glutaraldehyde (GA) in DI water was delivered and incubated for 2 h before wash (DI water) and a nitrogen blow dry, generating an aldehyde-activated surface with GA covalently linked to the amine groups. Subsequently, a saline solution (1× PBS) carrying mAbs ~25 μg/mL was delivered and incubated for 2 h, allowing mAbs to covalently link to the aldehyde groups, before a copious wash (1× PBS). This was followed by a wash with 100 mM ethanolamine in 1× PBS for 1 h to passivate unreacted aldehyde groups against nonspecific bindings. Distinct solutions of specific mAbs required for multiplexed detection were delivered through dedicated channels to the select regions of nanopores. Selective immobilization of FITC-labeled anti-cTnT within the active sites was confirmed *via* an epi-fluorescence microscope (Eclipse, Nikon, Japan) and the image was captured *via* a thermoelectric-cooled electron-multiplying charge-coupled device (EMCCD; iXon 3897, Andor, Dublin, Ireland).

***I − V* measurements.** Sample channels (8 μm wide) moulded into a PDMS slab and blocked by 1% BSA in 1× PBS were carefully aligned to include single nanopores exclusively and fastened in place by clamping. Sample and recording channels were all filled with the same electrolyte solution having the stated ionic strength and pH value. Metal wires (Ag/AgCl) were immersed into fluidic ports as the recording and reference (sample channels) electrodes and then connected to a patch-clamp amplifier (EPC10, HEKA Elektronik, Lambrecht, Germany). Patchmaster data acquisition software (HEKA)

was used to acquire $I-V$ curves by measuring the ionic currents for an applied voltage ramp from −1 V to +1 V in 50 mV increments for every 30 ms. For real-time current rectification data, $I-V$ curves were acquired for every 30 s. For human serum samples, $I-V$ measurements were taken after incubation with the sample (~20 min) and the subsequent elution with 0.01× PBS (~5 min). All measurements were conducted inside a Faraday cage to shield against any electromagnetic interference.

Corresponding Author

*To whom correspondence should be addressed. Phone: +852-2358 7068. Fax: +852-2358 1485. E-mail: eelyobas@ust.hk

Conflict of Interest: The authors declare no competing financial interests.

Acknowledgment. This work was financially supported by the Research Grant Council of Hong Kong under Grants 16203515 and 16209316.

Supporting Information Available: Figures for the device fabrication and experimental data: the nanopore conductance; the nanopore calibration curves for the cancer marker proteins independently introduced in the assay buffer; and the controls for the cross reactivity of mAbs. This material is available free of charge *via* the Internet at http://pubs.acs.org.

REFERENCES AND NOTES

1. Sander, C. Genomic Medicine and the Future of Health Care. *Science* **2000**, *287*, 1977−1978.

2. Etzioni, R.; Urban, N.; Ramsey, S.; McIntosh, M.; Schwartz, S.; Reid, B.; Radich, J.; Anderson, G.; Hartwell, L. The Case for Early Detection. *Nat. Rev. Cancer* **2003**, *3*, 243−252.

3. Wulfkuhle, J. D.; Liotta, L. A.; Petricoin, E. F. Proteomic Applications for the Early Detection of Cancer. *Nat. Rev. Cancer* **2003**, *3*, 267−275.

4. Ward, A. M.; Catto, J. W. F.; Hamdy, F. C. Prostate Specific Antigen: Biology, Biochemistry and Available Commercial Assays. *Ann. Clin. Biochem.* **2001**, *38*, 633−651.

5. Chou, S. F.; Hsu, W. L.; Hwang, J. M.; Chen, C. Y. Development of an Immunosensor for Human Ferritin, a Nonspecific Tumor Marker, Based on Surface Plasmon Resonance. *Biosens. Bioelectron.* **2004**, *19*, 999−1005.

6. Wu, G. H.; Datar, R. H.; Hansen, K. M.; Thundat, T.; Cote, R. J.; Majumdar, A. Bioassay of Prostate-Specific Antigen (PSA) Using Microcantilevers. *Nat. Biotechnol.* **2001**, *19*, 856−860.

7. Allen, B. L.; Kichambare, P. D.; Star, A. Carbon Nanotube Field-Effect-Transistor-Based Biosensors. *Adv. Mater.* **2007**, *19*, 1439−1451.

8. Cui, Y.; Wei, Q. Q.; Park, H. K.; Lieber, C. M. Nanowire Nanosensors for Highly Sensitive and Selective Detection of Biological and Chemical Species. *Science* **2001**, *293*, 1289−1292.

9. Zheng, G. F.; Patolsky, F.; Cui, Y.; Wang, W. U.; Lieber, C. M. Multiplexed Electrical Detection of Cancer Markers with Nanowire Sensor Arrays. *Nat. Biotechnol.* **2005**, *23*, 1294−1301.

10. Patolsky, F.; Zheng, G. F.; Hayden, O.; Lakadamyali, M.; Zhuang, X. W.; Lieber, C. M. Electrical Detection of Single Viruses. *Proc. Natl. Acad. Sci. U. S. A.* **2004**, *101*, 14017−14022.

11. Cheng, Y.; Chen, K. S.; Meyer, N. L.; Yuan, J.; Hirst, L. S.; Chase, P. B.; Xiong, P. Functionalized SnO_2 Nanobelt Field-Effect Transistor Sensors for Label-Free Detection of Cardiac Troponin. *Biosens. Bioelectron.* **2011**, *26*, 4538−4544.

12. Eijkel, J. C. T.; van den Berg, A. Nanofluidics: What Is It and What Can We Expect from It? *Microfluid. Nanofluid.* **2005**, *1*, 249−267.

13. Zhang, G. J.; Zhang, G.; Chua, J. H.; Chee, R. E.; Wong, E. H.; Agarwal, A.; Buddharaju, K. D.; Singh, N.; Gao, Z. Q.; Balasubramanian, N. DNA Sensing by Silicon Nanowire: Charge Layer Distance Dependence. *Nano Lett.* **2008**, *8*, 1066−1070.

14. Kim, S. J.; Song, Y. A.; Han, J. Nanofluidic Concentration Devices for Biomolecules Utilizing Ion Concentration Polarization: Theory, Fabrication, and Applications. *Chem. Soc. Rev.* **2010**, *39*, 912−922.

15. Cheng, L. J.; Guo, L. J. Nanofluidic Diodes. *Chem. Soc. Rev.* **2010**, *39*, 923−938.

16. Pu, Q. S.; Yun, J. S.; Temkin, H.; Liu, S. R. Ion-Enrichment and Ion-Depletion Effect of Nanochannel Structures. *Nano Lett.* **2004**, *4*, 1099−1103.

17. Siwy, Z.; Apel, P.; Baur, D.; Dobrev, D. D.; Korchev, Y. E.; Neumann, R.; Spohr, R.; Trautmann, C.; Voss, K. O. Preparation of Synthetic Nanopores with Transport Properties Analogous to Biological Channels. *Surf. Sci.* **2003**, *532*, 1061−1066.

18. Daiguji, H.; Oka, Y.; Shirono, K. Nanofluidic Diode and Bipolar Transistor. *Nano Lett.* **2005**, *5*, 2274−2280.

19. Cheng, L. J.; Guo, L. J. Rectified Ion Transport through Concentration Gradient in Homogeneous Silica Nanochannels. *Nano Lett.* **2007**, *7*, 3165−3171.

20. Ali, M.; Yameen, B.; Neumann, R.; Ensinger, W.; Knoll, W.; Azzaroni, O. Biosensing and Supramolecular Bioconjugation in Single Conical Polymer Nanochannels. Facile Incorporation of Biorecognition Elements into Nanoconfined Geometries. *J. Am. Chem. Soc.* **2008**, *130*, 16351−16357.

21. Perry, J. M.; Zhou, K. M.; Harms, Z. D.; Jacobson, S. C. Ion Transport in Nanofluidic Funnels. *ACS Nano* **2010**, *4*, 3897−3902.

22. Umehara, S.; Karhanek, M.; Davis, R. W.; Pourmand, N. Label-free Biosensing with Functionalized Nanopipette Probes. *Proc. Natl. Acad. Sci. U. S. A.* **2009**, *106*, 4611−4616.

23. Vlassiouk, I.; Kozel, T. R.; Siwy, Z. S. Biosensing with Nanofluidic Diodes. *J. Am. Chem. Soc.* **2009**, *131*, 8211−8220.

24. Ali, M.; Neumann, R.; Ensinger, W. Sequence-Specific Recognition of DNA Oligomer Using Peptide Nucleic Acid (PNA)-Modified Synthetic Ion Channels: PNA/DNA Hybridization in Nanoconfined Environment. *ACS Nano* **2010**, *4*, 7267−7274.

25. Ali, M.; Ramirez, P.; Nguyen, H. Q.; Nasir, S.; Cervera, J.; Mafe, S.; Ensinger, W. Single Cigar-Shaped Nanopores Functionalized with Amphoteric Amino Acid Chains: Experimental and Theoretical Characterization. *ACS Nano* **2012**, *6*, 3631−3640.

26. Ali, M.; Nasir, S.; Nguyen, Q. H.; Sahoo, J. K.; Tahir, M. N.; Tremel, W.; Ensinger, W. Metal Ion Affinity-Based Biomolecular Recognition and Conjugation inside

Synthetic Polymer Nanopores Modified with Iron-Terpyridine Complexes. *J. Am. Chem. Soc.* **2011**, *133*, 17307−17314.

27. Wang, J.; Hou, J.; Zhang, H. C.; Tian, Y.; Jiang, L. Single Nanochannel-Aptamer-Based Biosensor for Ultrasensitive and Selective Cocaine Detection. *ACS Appl. Mater. Interfaces* **2018**, *10*, 2033−2039.
28. Liu, Y. F.; Yobas, L. Label-Free Specific Detection of Femtomolar Cardiac Troponin Using an Integrated Nanoslit Array Fluidic Diode. *Nano Lett.* **2014**, *14*, 6983−6990.
29. Umehara, S.; Pourmand, N.; Webb, C. D.; Davis, R. W.; Yasuda, K.; Karhanek, M. Current Rectification with Poly-L-Lysine-Coated Quartz Nanopipettes. *Nano Lett.* **2006**, *6*, 2486−2492.
30. Liu, Q.; Wang, Y.; Guo, W.; Ji, H.; Xue, J.; Ouyang, Q. Asymmetric Properties of Ion Transport in a Charged Conical Nanopore. *Phys. Rev. E* **2007**, *75*, 051201.
31. Smeets, R. M. M.; Keyser, U. F.; Krapf, D.; Wu, M. Y.; Dekker, N. H.; Dekker, C. Salt Dependence of Ion Transport and DNA Translocation through Solid-State Nanopores. *Nano Lett.* **2006**, *6*, 89−95.
32. Stein, D.; Kruithof, M.; Dekker, C. Surface-Charge-Governed Ion Transport in Nanofluidic Channels. *Phys. Rev. Lett.* **2004**, *93*, 035901.
33. Behrens, S. H.; Grier, D. G. The Charge of Glass and Silica Surfaces. *J. Chem. Phys.* **2001**, *115*, 6716−6721.
34. Schoch, R. B.; Renaud, P. Ion Transport through Nanoslits Dominated by the Effective Surface Charge. *Appl. Phys. Lett.* **2005**, *86*, 253111.
35. Cao, Z.; Yobas, L. Induced Hydraulic Pumping *via* Integrated Submicrometer Cylindrical Glass Capillaries. *Electrophoresis* **2014**, *35*, 2353−2360.

36. Chua, J. H.; Chee, R. E.; Agarwal, A.; Wong, S. M.; Zhang, G. J. Label-Free Electrical Detection of Cardiac Biomarker with Complementary Metal-Oxide Semiconductor-Compatible Silicon Nanowire Sensor Arrays. *Anal. Chem.* **2009**, *81*, 6266−6271.

37. Huang, T. L.; Shieh, P. C. H.; Cooke, N. Isoelectric-Focusing of Proteins in Capillary Electrophoresis with Pressure-Driven Mobilization. *Chromatographia* **1994**, *39*, 543−548.

38. Karmali, A.; Novo, C. Human Alpha-Fetoprotein - Isolation and Production of Monoclonal-Antibodies. *Biochimie* **1990**, *72*, 369−374.

39. Hynes, N. E.; Stern, D. F. The Biology of ErbB-2/Neu/Her-2 and Its Role in Cancer. *Biochim. Biophys. Acta, Rev. Cancer* **1994**, *1198*, 165−184.

40. Casey, B. J.; Kofinas, P. Selective Binding of Carcinoembryonic Antigen Using Imprinted Polymeric Hydrogels. *J. Biomed. Mater. Res., Part A* **2008**, *87A*, 359−363.

41. Crandall, B. F.; Lau, H. L. Alpha-Fetoprotein - a Review. *Crit. Rev. Clin. Lab. Sci.* **1981**, *15*, 127−185.

42. Ouyang, W.; Han, J.; Wang, W. Enabling Electrical Biomolecular Detection in High Ionic Concentrations and Enhancement of the Detection Limit thereof by Coupling a Nanofluidic Crystal with Reconfigurable Ion Concentration Polarization. *Lab Chip* **2017**, *17*, 3772−3784.

For Table of Contents Only